

Measuring valley polarization in transition metal dichalcogenides with second-harmonic spectroscopy

Ho Yi Wei^{1,2,3}, Henrique G. Rosa², Ivan Verzhbitskiy^{2,3}, Manuel J. L. F. Rodrigues^{2,4}, Takashi Taniguchi⁵, Kenji Watanabe⁵, Goki Eda^{2,3,6}, Vitor M. Pereira^{2,3,‡}, José Carlos Viana Gomes^{2,3,§}

¹NUS Graduate School for Integrative Sciences and Engineering (NGS), University Hall, Tan Chin Tuan Wing, Level 4 #04-02, 21 Lower Kent Ridge, Singapore 119077

²Centre for Advanced 2D Materials and Graphene Research Centre, National University of Singapore, 6 Science Drive 2, Singapore 117546

³Department of Physics, National University of Singapore, 2 Science Drive 3, Singapore 117551

⁴Center of Physics and Department of Physics, Universidade do Minho, 4710-057, Braga, Portugal

⁵National Institute for Materials Science, 1-1 Namiki, Tsukuba 305-0044, Japan

⁶Department of Chemistry, National University of Singapore, 3 Science Drive 3, Singapore 117543

^{‡,§} Corresponding author email: vpereira@nus.edu.sg, phyvjc@nus.edu.sg

Keywords: valley polarization, valleytronics, transition metal dichalcogenides, molybdenum diselenide, second-harmonic generation, nonlinear optics

Abstract

Inducing a population imbalance at different valleys of an electronic system lowers its effective rotational symmetry. We introduce a technique to measure such valley imbalance (a valley polarization) that directly exploits this symmetry reduction as well as the unique fingerprints it has in the polarization-dependent second-harmonic generation. We describe the principle and detection scheme in the context of hexagonal two-dimensional crystals, which include graphene-based systems and the family of transition metal dichalcogenides. The technique is demonstrated on a MoSe₂ monolayer at room temperature. We include a model that shows the valley polarization-induced second-harmonic susceptibility is proportional to the effective valley imbalance, and one order of magnitude larger for quasi-resonant pump conditions versus off-resonant excitation. Importantly, we deliberately keep the setup as simple as possible, where a single laser beam simultaneously creates a controllable valley imbalance and pumps the second-harmonic process. In addition to providing the first experimental demonstration of the effect, this work establishes a conceptually very simple and compact way of measuring the instantaneous valley polarization, with direct applicability in valleytronics.

Introduction — In semiconductors, valleys refer to the local extrema of the electronic band structure in momentum space, i.e. local maxima (minima) of the valence (conduction) band. Valleytronics aims to manipulate the population of charge carriers in each valley such that there is a population imbalance between non-equivalent valleys, thereby establishing a valley polarization (VP) [1]. In addition to the charge (electronics) and spin (spintronics), the ability to induce, sustain, and control a valley polarization endows electrons with a new degree-of-freedom to encode information [1–3].

Systems involving one or a few layers of graphene or transition metal dichalcogenides (TMDs) are currently the forefront platforms where the promise of valleytronics is being most actively explored [4]. At the core of this drive is their unique electronic structure that features an underlying Diracness pinned at the two non-equivalent valleys ($+K$ and $-K$) enabled by the hexagonal crystal structure [5], each valley being endowed with a finite Berry curvature. Such key attributes are compounded by other practical properties such as their facile electrostatic tunability [6], strong and rich interaction with light [7], and the versatility that arises from combining different monolayers in more complex heterostructures [8]. These aspects have enabled the recent observation of valley Hall effect [9,10], or the optical excitation and quantum manipulation [11] of VP in this class of systems.

In structures lacking inversion symmetry (e.g. monolayer TMDs or biased bilayer graphene), the Berry curvature and orbital magnetic moment have the same magnitude but opposite sign at each of the $\pm K$ valleys. This gives rise to an optical selection rule that allows a convenient remote control over the electronic population in each valley by shining left (σ^-) or right (σ^+) circularly polarized light onto the sample [12,13].

A most basic and crucial requirement to support the development of valleytronics is the ability to detect and quantify the degree of VP on a sample with spatial resolution, instantaneously, and in a way that is non-invasive and expedite. Up to now, this has been approached using polarization-resolved photoluminescence (PL) [14–17] and the magneto-optic Kerr effect [18–20]. However, VP detection by PL requires the material to have a bandgap, is non-instantaneous by virtue of the PL

process, and probing VP lifetimes this way is limited by the excitonic recombination time [19,21]. On the other hand, for the Kerr effect to arise, the material needs to have a strong spin-orbit coupling so that a VP correlates with an out-of-plane magnetization [19,20,22,23]. Most significantly, both of these shortcomings in detecting VP by optical means impede their use in monolayer graphene which has neither a gap nor a relevant spin-orbit coupling [5].

Recent theoretical work proposed the use of second-harmonic generation (SHG) to probe VP and valley-polarized currents in graphene and TMDs [24–27]. It is well known that, being dictated by the second-order nonlinear electric susceptibility tensor, $\chi_{ijk}^{(2)}(\omega_i = \omega_j + \omega_k)$, SHG is a robust intrinsic feature of monolayer TMDs [28–31], but is absent in centrosymmetric crystals such as graphene or even-layered TMDs of the 2H polytype. More specifically, the non-vanishing components of $\chi^{(2)}$ are fundamentally constrained by the point group symmetry of the crystal which, in the class of graphene and hexagonal TMDs at equilibrium, implies that the intrinsic SHG is defined by a single number: $\chi_{\text{int}} \equiv \chi_{222}^{(2)} = -\chi_{211}^{(2)} = -\chi_{121}^{(2)} = -\chi_{112}^{(2)} \neq 0$ [32,33]. However, an imbalance of electronic population at different valleys lowers the effective rotational symmetry of the electronic system with respect to the crystal's point group. This brings about additional non-zero components of $\chi^{(2)}$ that would otherwise be forbidden (namely, $\chi_{\text{vp}} \equiv \chi_{111}^{(2)} = -\chi_{122}^{(2)} = -\chi_{212}^{(2)} = -\chi_{221}^{(2)} \neq 0$, $\chi_{111}^{(2)} \neq \chi_{222}^{(2)}$) and, as a result, changes the material's SHG fingerprint in a way that can be directly related to the induced VP. For example, if the VP is the result of a difference $\Delta\mu$ in the electronic chemical potential at each valley, it can be shown that, to lowest order, the magnitude of $\chi_{\text{vp}}^{(2)}$ increases linearly with $\Delta\mu$ [24,26,34]. More generically, defining the degree of VP as $P_v \equiv (N_+ - N_-)/(N_+ + N_-)$, where N_{\pm} is the population at the $\pm K$ valley, one can say that $\chi_{\text{vp}}(P_v) \propto P_v$ whereas χ_{int} is independent of P_v .

When both present, the two contributions to the SHG, χ_{int} and χ_{vp} , may be distinguished by polarization spectroscopy since, physically, their associated nonlinear polarization is directed along

orthogonal directions. More interestingly, in the case of graphene and other centrosymmetric crystals where $\chi_{\text{int}} = 0$ by symmetry, gauging VP with SHG is even easier because this nonlinear effect is only a result of χ_{vp} . Thus, SHG spectroscopy can be a powerful tool in graphene valleytronics. This is relevant because, recently, it has been experimentally demonstrated that spin-valley currents can be injected from TMD into graphene at room temperature [35,36]. Moreover, SHG is sensitive to the instantaneous degree of VP, making it particularly suitable to characterize the fast valley relaxation processes [11] and to operate at room temperature, where techniques based on PL stand at a disadvantage [19].

In this context, this paper reports the first experimental demonstration of SHG as an effective tool to probe VP at room temperature. In a home-built multiphoton microscope, a molybdenum diselenide (MoSe₂) sample (2H polytype) is illuminated by a single laser beam which acts as both SHG and VP pump. By continuously varying the ellipticity of the incoming polarization from linear to circular, we observe the progressive development of χ_{vp} which, added to the flake's intrinsic SHG contribution, causes a well-defined rotation of the polarization-resolved SHG pattern at equilibrium [31,37,38]. This rotation directly yields the magnitude of χ_{vp} . Furthermore, we build a model encompassing steady-state and transient rate equations of the exciton population on each valley to describe both the non-saturated and saturated valley pumping regimes, which is in good agreement with our experimental data.

Polarized second-harmonic generation — If linearly polarized light is used to pump the SHG process, assuming the electric field vector is contained in the crystal plane, the second-order nonlinear polarization is given by [26]

$$\begin{bmatrix} P_{ZZ} \\ P_{AC} \end{bmatrix} \propto \begin{bmatrix} \chi_{\text{vp}}(P_v) & -\chi_{\text{vp}}(P_v) & -\chi_{\text{int}} \\ -\chi_{\text{int}} & \chi_{\text{int}} & -\chi_{\text{vp}}(P_v) \end{bmatrix} \begin{bmatrix} E_{ZZ}^2 \\ E_{AC}^2 \\ 2E_{ZZ}E_{AC} \end{bmatrix}, \quad (1)$$

where E_{ZZ} and E_{AC} are the pump electric fields along the zig-zag (ZZ) and armchair (AC) directions, respectively. This form of the $\chi^{(2)}$ tensor applies to crystals with non-centrosymmetric D_{3h} ($\chi_{\text{int}} \neq 0$) and centrosymmetric D_{6h} ($\chi_{\text{int}} = 0$) point groups. A simple inspection of Equation (1) shows that the total SHG signal is independent on the pump field polarization angle. However, if the SHG signal is analyzed before detection with a polarizer aligned in the same direction β as the pump field, the signal is $S(\beta, P_v) \propto |\chi_{\text{int}} \sin(3\beta) - \chi_{\text{vp}}(P_v) \cos(3\beta)|^2$, which explicitly depends on both the intrinsic and VP-induced contributions to $\chi^{(2)}$. One can easily see that the pattern described by $S(\beta, P_v)$ as a function of β corresponds to a scaling and rotation of the six-fold pattern we have for $P_v = 0$ (see Figure 1a), where the offset angle, Δ' , is given by

$$\Delta' \approx \frac{1}{3} \frac{\chi_{\text{vp}}(P_v)}{\chi_{\text{int}}} \cos \phi \quad (2)$$

Here, ϕ is the phase difference between the two contributions to $\chi^{(2)}$, defined from $e^{i\phi} = \chi_{\text{vp}}(P_v)/\chi_{\text{int}}$, which depends on the detuning of the pump field from the exciton transitions, and should be close to zero. Equation (2) gives a very intuitive way to detect VP, illustrated in Figure 1a (additional details provided in the Supplementary Information).

Another way to conduct this experiment is to hold the polarization of the incoming light fixed while rotating the analyzer alone. We adopted this strategy for the data presented here because the experimental setup is further simplified and, more importantly, the offset angle in this case reads

$$\Delta \approx \frac{\chi_{\text{vp}}(P_v)}{\chi_{\text{int}}} \cos \phi \quad (3)$$

The difference by a factor of 3 in comparison with the result (2) translates into a three-fold increase in experimental sensitivity.

A home-built multiphoton transmission microscope was used for the polarization-resolved second-harmonic generation experiment (Figure 1b) [31]. A pulsed laser beam (wavelength: 780/1560 nm, pulse duration: 200 fs, repetition rate: 80 MHz) simultaneously pumps VP and SHG. This is possible because the laser polarization ellipticity (γ) is varied by a set of polarizers and waveplates, from linear (required to pump SHG) to circular (required to pump VP). At the sample, the pump laser with average power ~ 1 to 5 mW was focused by a 100 \times objective down to spot diameter of 1 μm (2 μm) for the 780 nm (1550 nm) pump. Throughout the experiment, the linear polarization angle (α) is kept constant and aligned to the AC direction of the sample, while γ is varied from -30° to 30° (Figure 1c). For each set of $\{\alpha, \gamma\}$, the analyzer is rotated 360° to analyze the SHG signal before reaching a spectrometer.

Furthermore, in order to characterize the impact of being near- and off-resonance with the excitonic transition energies of MoSe₂, we have analyzed the results of pumping at two different wavelengths: $\lambda_p = 1560$ nm (0.80 eV, for sub-bandgap excitation) and 780 nm (1.59 eV, for excitation quasi-resonant with the A exciton, ~ 19 meV above its photoluminescence peak, see Supplementary Information).

Two-level system model — To better understand the role of the valley-imbalanced electronic populations and be able to estimate their contribution to the total SHG signal, we elaborated a two-level system model to describe the electronic populations in the $\pm\text{K}$ valleys (see Supplementary Information for details).

To quantitatively obtain Δ , we start from a pair of 2-level systems to model $\pm\text{K}$ valleys, as shown in Figure S3, with rate equations of population N_\pm in the $\pm\text{K}$ valleys

$$\frac{dN_\pm}{dt} = -\Gamma N_\pm - AN_\pm^2 - \frac{I_\pm}{2 I_{\text{sat}}} \Gamma (N_\pm - N_{0,\pm}) \pm \Gamma_v (N_\mp - N_\pm) \quad (4)$$

$$N_{\pm} + N_{0,\pm} = N_T$$

where Γ = recombination rate, A = exciton-exciton annihilation rate, Γ_v = intervalley recombination rate, I_{\pm} = intensity of σ^{\pm} , I_{sat} = saturation intensity of MoSe₂ and N_T = total excitonic density.

Initially, we solved Equation (4) in steady-state regime with $A = 0$ to obtain population imbalance, ΔN_{SS} :

$$\Delta N \equiv N_+ - N_-$$

$$\Delta N_{SS} = N_T \frac{2\eta \sin 2\gamma}{(2 + \eta)^2 - (\eta \sin 2\gamma)^2} \quad (5)$$

where $\eta = (I_+ + I_-)/I_{\text{sat}}$ is the intensity saturation parameter and γ is the ellipticity of the pump laser beam. This steady-state solution is a good model for pump intensities below or comparable to I_{sat} (see Supplementary Information). However, in our experiments, the pump intensities are much larger than I_{sat} , causing a temporal mismatch between transient ΔN and laser intensity, as shown in Figure 2a. To account for this, we also solved Equation (4) numerically with $\Gamma = 1/3 \text{ ps}^{-1}$ (at room temperature) [21], $A = 0.33 \text{ cm}^2 \text{ s}^{-1}$ [39], $\Gamma_v = 0$ (both pump energies are below the threshold for phonon coupling [17]), $I_{\text{sat}} = 2.5 \text{ MW cm}^{-2}$ [40] and 11.6 MW cm^{-2} [41,42] for pump wavelength λ_p of 780 nm and 1560 nm, respectively. Figure 2 shows the results of the transient solution.

The effective population imbalance, ΔN_{eff} , is obtained by

$$\Delta N_{\text{eff}} = \int_{-\infty}^{\infty} \Delta N(t) I(t) dt$$

$$I(t) = \frac{2}{\tau} \sqrt{\frac{\ln 2}{\pi}} e^{-4 \ln 2 \left(\frac{t}{\tau}\right)^2} \quad (6)$$

where τ is the pulse duration full width at half maximum and $\Delta N(t)$ is the instantaneous ΔN . We normalize ΔN because our VP pump beam is also the VP probe, and the $\Delta N(t)$ varies rapidly around the probe pulse, thus ΔN_{eff} is the temporally-windowed ΔN that is being sensed (see Supplementary

Information 2). From the η used in the experiment (Figure 2b) we fit it to the experimental data to obtain the proportionality relationship between intrinsic and valley polarization-induced susceptibilities by using the equations:

$$\frac{\Delta N_{\text{eff}}}{N_T} = K \frac{2\eta' \sin 2a\gamma}{(2 + \eta')^2 - (\eta' \sin 2a\gamma)^2}$$

$$\Delta = \frac{1}{2} \tan^{-1} \left[2 \frac{\chi_{\text{vp}}/\chi_{\text{int}}}{(\chi_{\text{vp}}/\chi_{\text{int}})^2 - 1} \right] \quad (7)$$

$$\frac{\chi_{\text{vp}}}{\chi_{\text{int}}} = k \Delta N_{\text{eff}}$$

where K and a are fitting parameters to adjust the steady-state ΔN_{eff} , to accommodate into transient solution, and η' is a fitting parameter for the saturation level. For $\eta \gg 1$, their values are

$$K = 1.058, a = 1.028, \log \eta' = 1.04, \log \eta = 1.41 \quad (8)$$

Results and discussion — The experimental results shown in Figure 3 are fitted to the model presented in Equation (7) using ΔN_{eff} obtained from calculation (Figure 2b), yielding fitting parameters $k_{1560} = -(0.21 \pm 0.02)/N_{T,1560}$ and $k_{780} = -(1.10 \pm 0.07)/N_{T,780}$ for $\lambda_p = 1560$ nm and 780 nm, respectively, where $N_{T,\lambda}$ is the total excitonic density for each pump wavelength λ . Uncertainties were obtained from fitting error, which is an underestimation.

From Figure 3, uncertainty is generally larger at large γ , which is anticipated because as the SHG signal becomes more circularly polarized, maximum SHG angle becomes less well-defined. This is a consequence for using a single beam to both pump and probe VP of MoSe₂ simultaneously.

Another consequence of using single beam is that the steady-state model fails because of high pump intensity ($\eta \gg 1$), which is needed for SHG. From Figure 2a, N_{\pm} (orange curves) saturates before the peak of I_{\pm} (blue curves), with N_+ (N_-) saturates before N_- (N_+) for $\gamma > 0$ ($\gamma < 0$) as $I_+ > I_-$ ($I_- > I_+$). This results in a transient population imbalance (red curve) that peaks before the probe beam, which is also the pump beam in our case, causing a reduction in the ΔN being measured

(ΔN_{eff} , green curve). This is further shown in Figure S6b, where $\eta' \ll \eta$ indicates a reduction in the effective VP pump intensity for $\eta \gg 1$; for $\eta \ll 1$, our simple transient model recovers steady-state result with $\eta' = \eta$ as shown in Figure S6b.

We also note that the uncertainties of k_λ are underestimated because k_λ depends on $\eta = I_{\text{peak}}/I_{\text{sat}}$. From literature, which is where we obtained I_{sat} , it could vary by few factors (for example, $I_{\text{sat}} = 3.4$ and 19.8 MW/cm² from [41] and [42], respectively) depending on the sample condition.

Conclusion — In this paper we showed that SHG can be used to probe VP in MoSe₂ at room temperature. Compared to existing techniques, SHG is more robust against material dependency (i.e. requirement of bandgap for PL and spin-orbital splitting for Kerr rotation) and is a more direct VP measurement (i.e. χ_{vp} arises from inversion symmetry breaking in momentum space). These advantageous make SHG a perfect tool to probe VP in monolayer graphene, and therefore a crucial steps towards realization of graphene valleytronics and valleytronics in general.

Acknowledgement — H. Y. W. acknowledges scholarship support from NGS. G.E. acknowledges financial support from National Research Foundation of Singapore (NRF Research Fellowship NRF-NRFF2011-02 and medium-sized centre programme) and Ministry of Education of Singapore (AcRF Tier 2 MOE2015-T2-2-123). V. M. P. acknowledges financial support from Ministry of Education of Singapore (FRC AcRF Tier 1 R-144-000-386-114). J. C. V. G. acknowledges financial support from CA2DM through National Research Foundation of Singapore (NRF-CRP Grant No. R-144-000-295-281).

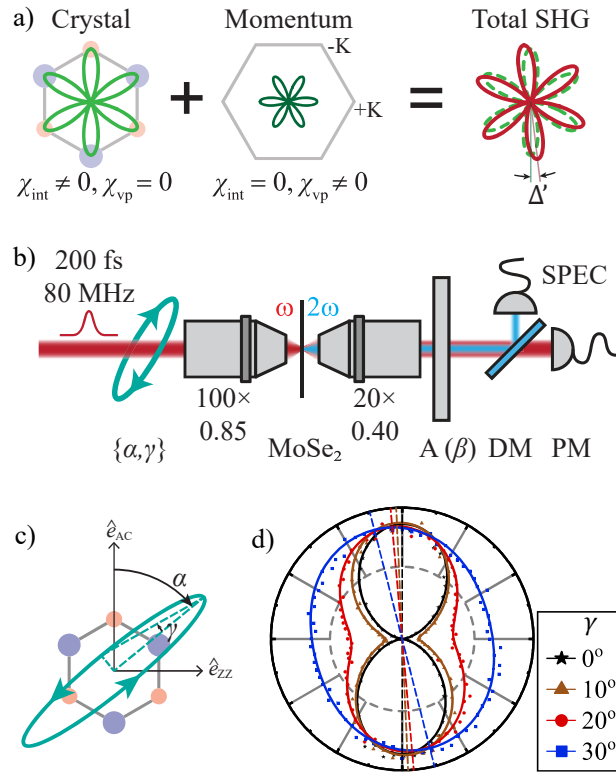


Figure 1: a) SHG contribution from crystal- and momentum-space inversion asymmetry. Signature of VP is when there is a small offset angle (Δ') of total SHG with respect to crystal contribution. b) Experimental setup. MoSe₂ sample is pumped by a 200 fs pulsed laser with elliptical polarization. DM = dichroic mirror; PM = power meter, for reference; SPEC = spectrometer. c) The elliptical polarization is parametrized by α and γ , which are the angle of the linear component from the AC direction and degree of ellipticity, respectively. d) Typical data for $\lambda_p = 780$ nm for various γ .

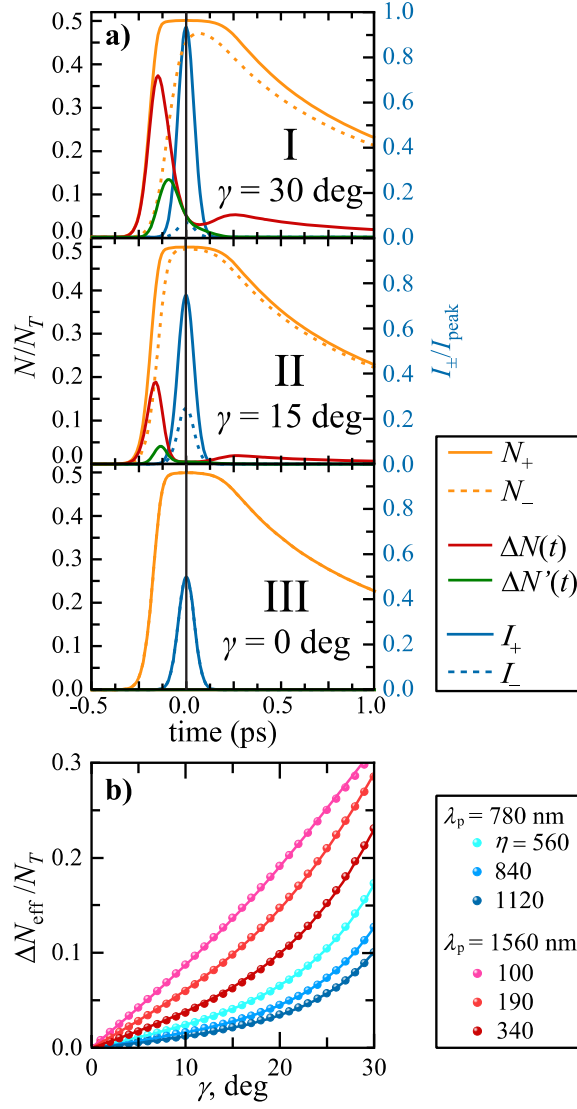


Figure 2: a) Calculation of electronic populations in +K (N_+ , solid orange curve) and -K (N_- , dashed orange curve) valleys for $\Gamma = 1/3 \text{ ps}^{-1}$, $A = 0.33 \text{ cm}^2 \text{ s}^{-1}$, $\Gamma_v = 0$, $\eta = 1120$ and γ of I) 30° , II) 15° and III) 0° . I_+ (solid blue curve) and I_- (dashed blue curve) are the σ^+ and σ^- component of the laser pulse intensities, respectively. Instantaneous population imbalance $\Delta N(t)$ is plotted in red curve, while those being experienced by the laser pulse is plotted in green curve ($\Delta N'(t) = \Delta N(t)I(t)$). There are only 2 graphs visible in III) because it is linearly polarized ($\gamma = 0$), thus the I_{\pm} and N_{\pm} graphs overlap and $\Delta N = 0$. b) Calculation summary of population imbalance as a function of γ for the intensities used in the experiments for different intensity saturation parameter (η). It is an odd function for γ .

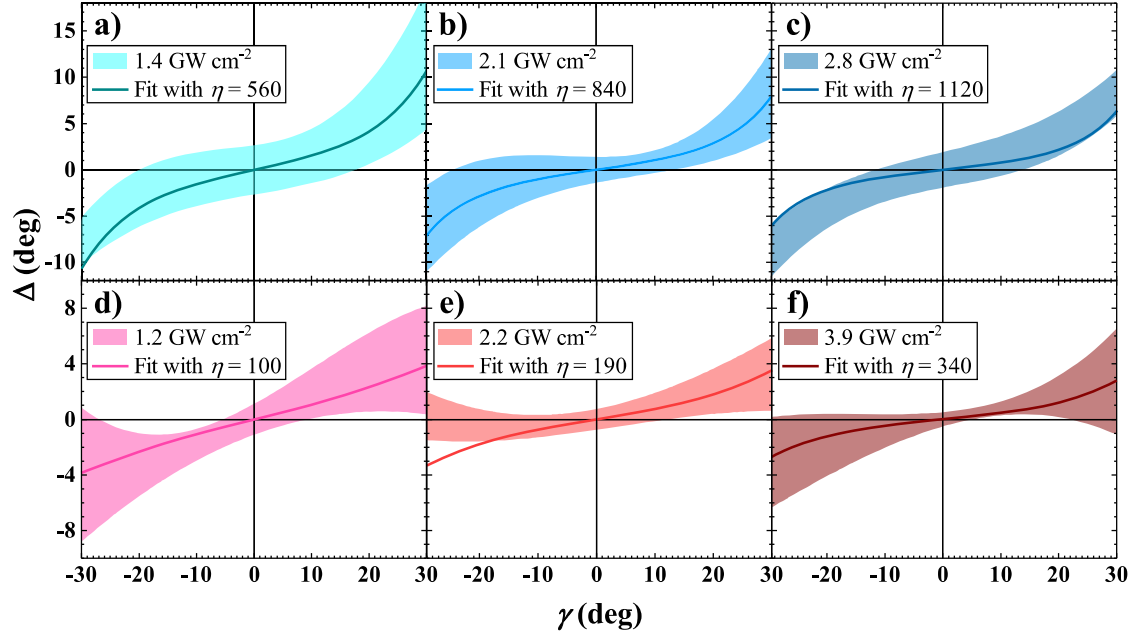


Figure 3: Angle of maximum SHG shift from that of without VP (Δ) against degree of ellipticity (γ) for λ_p of 780 nm (a-c) and 1560 nm (d-f) and different pump intensities (shaded areas, edges are the upper/lower limits of uncertainties, accounting for fitting error and standard deviation, while centers are the mean data). Larger Δ indicates more ΔN . Data obtained at room temperature. The data are fitted to ΔN_{eff} obtained from model below using respective intensity ratio η (solid lines).

References

1. A. Rycerz, J. Tworzydło, and C. W. J. Beenakker, "Valley filter and valley valve in graphene," *Nat. Phys.* **3**, 172–175 (2007).
2. O. Gunawan, Y. P. Shkolnikov, K. Vakili, T. Gokmen, E. P. De Poortere, and M. Shayegan, "Valley Susceptibility of an Interacting Two-Dimensional Electron System," *Phys. Rev. Lett.* **97**, 186404 (2006).
3. Y. S. Ang, S. A. Yang, C. Zhang, Z. Ma, and L. K. Ang, "Valleytronics in merging Dirac cones: All-electric-controlled valley filter, valve, and universal reversible logic gate," *Phys. Rev. B* **96**, 245410 (2017).
4. J. R. Schaibley, H. Yu, G. Clark, P. Rivera, J. S. Ross, K. L. Seyler, W. Yao, and X. Xu, "Valleytronics in 2D materials," *Nat. Rev. Mater.* **1**, 16055 (2016).
5. K. S. Novoselov, A. K. Geim, F. Guinea, N. M. R. Peres, and A. H. Castro Neto, "The electronic properties of graphene," *Rev. Mod. Phys.* **81**, 109–162 (2009).
6. S. Manzeli, D. Ovchinnikov, D. Pasquier, O. V. Yazyev, and A. Kis, "2D transition metal dichalcogenides," *Nat. Rev. Mater.* **2**, 17033 (2017).
7. K. F. Mak and J. Shan, "Photonics and optoelectronics of 2D semiconductor transition metal dichalcogenides," *Nat. Photonics* **10**, 216–226 (2016).
8. X. Xu, W. Yao, D. Xiao, and T. F. Heinz, "Spin and pseudospins in layered transition metal dichalcogenides," *Nat. Phys.* **10**, 343–350 (2014).
9. K. F. Mak, K. L. McGill, J. Park, and P. L. McEuen, "The valley Hall effect in MoS₂ transistors," *Science* **344**, 1489–1492 (2014).
10. J. Lee, K. F. Mak, and J. Shan, "Electrical control of the valley Hall effect in bilayer MoS₂ transistors," *Nat. Nanotechnol.* **11**, 421–425 (2016).
11. K. F. Mak, D. Xiao, and J. Shan, "Light–valley interactions in 2D semiconductors," *Nat.*

- Photonics **12**, 451–460 (2018).
12. X. Xu, W. Yao, D. Xiao, and T. F. Heinz, "Spin and pseudospins in layered transition metal dichalcogenides," *Nat. Phys.* **10**, 343–350 (2014).
 13. W. Yao, D. Xiao, and Q. Niu, "Valley-dependent optoelectronics from inversion symmetry breaking," *Phys. Rev. B* **77**, 235406 (2008).
 14. T. Cao, G. Wang, W. Han, H. Ye, C. Zhu, J. Shi, Q. Niu, P. Tan, E. Wang, B. Liu, and J. Feng, "Valley-selective circular dichroism of monolayer molybdenum disulphide," *Nat. Commun.* **3**, 887 (2012).
 15. H. Zeng, J. Dai, W. Yao, D. Xiao, and X. Cui, "Valley polarization in MoS₂ monolayers by optical pumping," *Nat. Nanotechnol.* **7**, 490–493 (2012).
 16. K. F. Mak, K. He, J. Shan, and T. F. Heinz, "Control of valley polarization in monolayer MoS₂ by optical helicity," *Nat. Nanotechnol.* **7**, 494–498 (2012).
 17. G. Kioseoglou, A. T. Hanbicki, M. Currie, A. L. Friedman, and B. T. Jonker, "Optical polarization and intervalley scattering in single layers of MoS₂ and MoSe₂," *Sci. Rep.* **6**, 25041 (2016).
 18. C. R. Zhu, K. Zhang, M. Glazov, B. Urbaszek, T. Amand, Z. W. Ji, B. L. Liu, and X. Marie, "Exciton valley dynamics probed by Kerr rotation in WSe₂ monolayers," *Phys. Rev. B* **90**, 161302 (2014).
 19. W.-T. Hsu, Y.-L. Chen, C.-H. Chen, P.-S. Liu, T.-H. Hou, L.-J. Li, and W.-H. Chang, "Optically initialized robust valley-polarized holes in monolayer WSe₂," *Nat. Commun.* **6**, 8963 (2015).
 20. T. Yan, S. Yang, D. Li, and X. Cui, "Long valley relaxation time of free carriers in monolayer WSe₂," *Phys. Rev. B* **95**, 241406 (2017).
 21. G. Wang, E. Palleau, T. Amand, S. Tongay, X. Marie, and B. Urbaszek, "Polarization and time-resolved photoluminescence spectroscopy of excitons in MoSe₂ monolayers," *Appl. Phys. Lett.* **106**, 112101 (2015).

22. Y. K. Kato, R. C. Myers, A. C. Gossard, and D. D. Awschalom, "Observation of the spin hall effect in semiconductors," *Science* **306**, 1910–1913 (2004).
23. J. Lee, K. F. Mak, and J. Shan, "Electrical control of the valley Hall effect in bilayer MoS₂ transistors," *Nat. Nanotechnol.* **11**, 421–425 (2016).
24. T. O. Wehling, A. Huber, A. I. Lichtenstein, and M. I. Katsnelson, "Probing of valley polarization in graphene via optical second-harmonic generation," *Phys. Rev. B* **91**, 041404 (2015).
25. J. Cheng, D. Huang, T. Jiang, Y. Shan, Y. Li, S. Wu, and W.-T. Liu, "Chiral selection rules for multi-photon processes in two-dimensional honeycomb materials," arXiv:1902.03401 (2019).
26. F. Hipolito and V. M. Pereira, "Second harmonic spectroscopy to optically detect valley polarization in 2D materials," *2D Mater.* **4**, 021027 (2017).
27. Y. K. Luo, J. Xu, T. Zhu, G. Wu, E. J. McCormick, W. Zhan, M. R. Neupane, and R. K. Kawakami, "Opto-valleytronic spin injection in monolayer MoS₂/few-layer graphene hybrid spin valves," *Nano Lett.* **17**, 3877–3883 (2017).
28. Y. Li, Y. Rao, K. F. Mak, Y. You, S. Wang, C. R. Dean, and T. F. Heinz, "Probing symmetry properties of few-layer MoS₂ and h-BN by optical second-harmonic generation," *Nano Lett.* **13**, 3329–3333 (2013).
29. N. Kumar, S. Najmaei, Q. Cui, F. Ceballos, P. M. Ajayan, J. Lou, and H. Zhao, "Second harmonic microscopy of monolayer MoS₂," *Phys. Rev. B* **87**, 161403(R) (2013).
30. H. G. Rosa, L. Junpeng, L. C. Gomes, M. J. L. F. Rodrigues, S. C. Haur, and J. C. V Gomes, "Second-Harmonic Spectroscopy for Defects Engineering Monitoring in Transition Metal Dichalcogenides," *Adv. Opt. Mater.* **6**, 1701327 (2018).
31. H. G. Rosa, Y. W. Ho, I. Verzhbitskiy, M. J. F. L. Rodrigues, T. Taniguchi, K. Watanabe, G. Eda, V. M. Pereira, and J. C. V Gomes, "Characterization of the second- and third-harmonic optical susceptibilities of atomically thin tungsten diselenide," *Sci. Rep.* **8**, 10035 (2018).

32. Y. R. Shen, *The Principles of Nonlinear Optics* (Wiley, 2003).
33. R. W. Boyd, *Nonlinear Optics*, 3rd ed. (Academic Press, 2008).
34. L. E. Golub and S. A. Tarasenko, "Valley polarization induced second harmonic generation in graphene," *Phys. Rev. B* **90**, 201402 (2014).
35. Y. K. Luo, J. Xu, T. Zhu, G. Wu, E. J. McCormick, W. Zhan, M. R. Neupane, and R. K. Kawakami, "Opto-valleytronic spin injection in monolayer MoS₂/few-layer graphene hybrid spin valves," *Nano Lett.* **17**, 3877–3883 (2017).
36. C. K. Safeer, J. Ingla-Aynés, F. Herling, J. H. Garcia, M. Vila, N. Ontoso, M. R. Calvo, S. Roche, L. E. Hueso, and F. Casanova, "Room-Temperature Spin Hall Effect in Graphene/MoS₂ van der Waals Heterostructures," *Nano Lett.* **19**, 1074–1082 (2019).
37. A. Autere, H. Jussila, Y. Dai, Y. Wang, H. Lipsanen, and Z. Sun, "Nonlinear Optics with 2D Layered Materials," *Adv. Mater.* **30**, 1705963 (2018).
38. A. Autere, H. Jussila, A. Marini, J. R. M. Saavedra, Y. Dai, A. Säynätjoki, L. Karvonen, H. Yang, B. Amirsolaimani, R. A. Norwood, N. Peyghambarian, H. Lipsanen, K. Kieu, F. J. G. de Abajo, and Z. Sun, "Optical harmonic generation in monolayer group-VI transition metal dichalcogenides," *Phys. Rev. B* **98**, 115426 (2018).
39. N. Kumar, Q. Cui, F. Ceballos, D. He, Y. Wang, and H. Zhao, "Exciton-exciton annihilation in MoSe₂ monolayers," *Phys. Rev. B* **89**, 125427 (2014).
40. Z. Nie, C. Trovatiello, E. A. A. Pogna, S. Dal Conte, P. B. Miranda, E. Kelleher, C. Zhu, I. C. E. Turcu, Y. Xu, K. Liu, G. Cerullo, and F. Wang, "Broadband nonlinear optical response of monolayer MoSe₂ under ultrafast excitation," *Appl. Phys. Lett.* **112**, 031108 (2018).
41. R. I. Woodward, R. C. T. Howe, T. H. Runcorn, G. Hu, F. Torrisi, E. J. R. Kelleher, and T. Hasan, "Wideband saturable absorption in few-layer molybdenum diselenide (MoSe₂) for Q-switching Yb-, Er- and Tm-doped fiber lasers," *Opt. Express* **23**, 20051 (2015).
42. Z. Luo, Y. Li, M. Zhong, Y. Huang, X. Wan, J. Peng, and J. Weng, "Nonlinear optical absorption of few-layer molybdenum diselenide (MoSe₂) for passively mode-locked soliton

fiber laser [Invited]," Photonics Res. **3**, A79 (2015).

Measuring valley polarization in transition metal dichalcogenides with second-harmonic spectroscopy

Ho Yi Wei^{1,2,3*}, Henrique G. Rosa^{2*}, Ivan Verzhbitskiy^{2,3}, Manuel J. L. F. Rodrigues^{2,4}, Takashi Taniguchi⁵, Kenji Watanabe⁵, Goki Eda^{2,3,4}, Vitor M. Pereira^{2,3,Φ}, José Carlos Viana Gomes^{2,3,Δ}

¹NUS Graduate School for Integrative Sciences and Engineering (NGS), University Hall, Tan Chin Tuan Wing, Level 4 #04-02, 21 Lower Kent Ridge, Singapore 119077

²Centre for Advanced 2D Materials (CA2DM), National University of Singapore, 6 Science Drive 2, Singapore 117546

³Department of Physics, National University of Singapore, 2 Science Drive 3, Singapore 117551

⁴Center of Physics and Department of Physics, Universidade do Minho, 4710-057, Braga, Portugal

⁵National Institute for Materials Science, 1-1 Namiki, Tsukuba 305-0044, Japan

⁶Department of Chemistry, National University of Singapore, 3 Science Drive 3, Singapore 117543

*These authors contributed equally to this work

ΦCorresponding author email: vpereira@nus.edu.sg

ΔCorresponding author email: phyvjc@nus.edu.sg

Contents

1	Sample fabrication and characterization.....	3
2	Detailed data analysis	3
3	Conventional polarized second-harmonic generation.....	4
4	Nonlinear optical susceptibilities.....	5
5	SH offset angle model.....	5
5.1	Steady-state solution	7
5.1.1	Steady-state solution with $A \neq 0$	7
5.2	Transient solution.....	7
6	References.....	13

1 Sample fabrication and characterization

The sample used in this work is a mechanically exfoliated monolayer molybdenum disulfide (MoSe_2) flake transferred onto fused silica substrate. In order to insulate the MoSe_2 sample from the environment, it was covered with a 20 nm thick flake of hexagonal-boron-nitride (hBN). Basic characterizations of the sample, such as optical microscopy, Raman spectroscopy and photoluminescence spectroscopy, are shown in Figure S1.

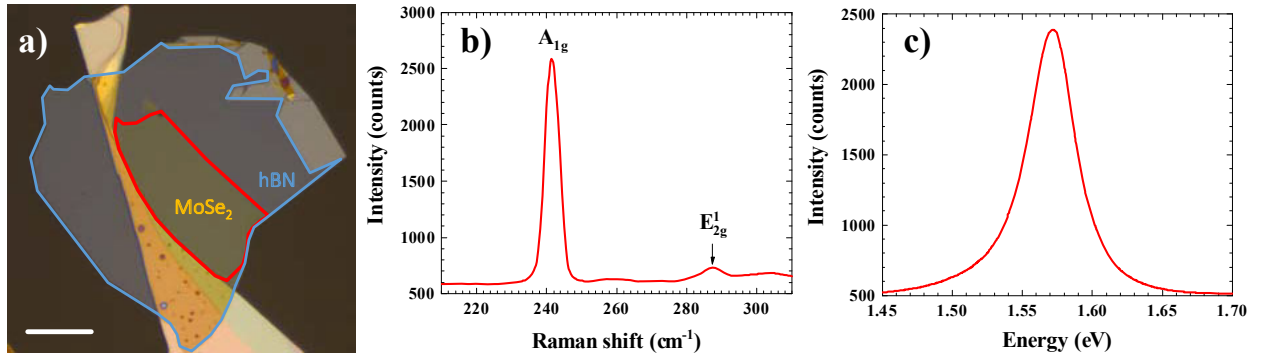


Figure S1: MoSe_2 flake characterization: a) Optical microscopy image – scale bar = 25 μm , b) Raman spectrum and c) photoluminescence spectrum (PL emission peak = 1.571 eV).

From Figure S1c, it is possible to observe that the photon energy in the test experiment, $E_{\text{photon}} = 1.590$ eV, is slightly higher (19 meV) than the optical bandgap energy, shown by the PL emission peak at 1.571 eV, while another photon energy $E_{\text{photon}} \sim 0.8$ eV is much smaller compared to the optical bandgap.

2 Detailed data analysis

To obtain actual γ , the pump data (e.g. Figure 3a in main text) are globally fitted to

$$I_{\text{pump}} = \frac{I_0}{2} [1 + \cos(2(\alpha_0 - \beta)) \cos(2\gamma)]$$

with I_0 and α_0 being the global variables. Here, I_0 is a normalizing factor for the intensities.

Meanwhile, the SHG data (e.g. Figure 3b in main text) are fitted to

$$I_{\text{SHG}} = I_0[\cos^2(\beta - \beta_{\text{max}}) + R \sin^2(\beta - \beta_{\text{max}})]$$

where $R = \frac{\text{minimum intensity}}{\text{maximum intensity}}$. Next, from our model (described below or in the main text) with the

assumption of no VP, we can infer $\beta_{\text{max}}(\chi_{\text{vp}} = 0) = 0$. Therefore, a shift in SHG maximum angle

$\Delta = \beta_{\text{max}}(\chi_{\text{vp}} \neq 0) - \beta_{\text{max}}(\chi_{\text{vp}} = 0) \neq 0$ indicates the presence of VP.

3 Conventional polarized second-harmonic generation

Prior experimental data presented in the main text, we performed polarization-resolved SHG (pSHG), whereby SHG power was measured co-linear to its excitation polarization, in order to get the AC direction of our sample, which is crucial for the experiment in the main text. Besides, we also measured pSHG for γ in the range of -30° to $+30^\circ$, and observed the similar trend (Δ' increases with γ) as the results in main text. Furthermore, $\frac{\Delta}{\Delta'} \approx 3$, which is consistent with the model below.

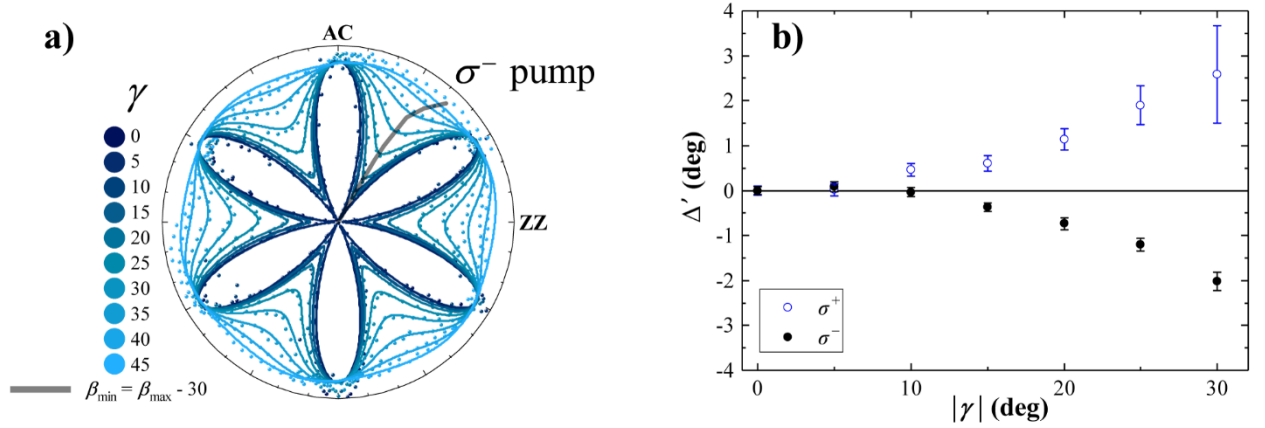


Figure S2: Conventional pSHG scheme. a) 6-fold symmetry of pSHG of MoSe₂ for γ in the range of 0 to 30°. Grey line as a guide for eye for the minimum SHG angle across γ . b) Maximum SHG angle offset compared to $\gamma = 0$ against γ for both σ^+ (dotted) and σ^- (solid) pump excitation. Here we use Δ' to distinguish with Δ in the main text.

4 Nonlinear optical susceptibilities

The χ_{int} and χ_{vp} are the intrinsic and valley polarization second-order susceptibilities are defined as:

$$\chi_{\text{int}} \equiv \chi_{111} = -\chi_{122} = -\chi_{212} = -\chi_{221}$$

$$\chi_{\text{vp}} \equiv \chi_{222} = -\chi_{211} = -\chi_{121} = -\chi_{112}$$

where 1 and 2 axes are the in ZZ and AC directions.

5 SH offset angle model

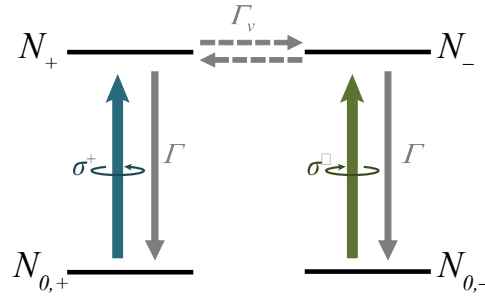


Figure S3: A pair of 2-level system to model dynamic of $\pm K$ valleys.

Considering a pair of 2-level systems (Figure S3) with 2 degenerated excited states representing $\pm K$ valleys (N_+ and N_-) and their ground states ($N_{0,+}$ and $N_{0,-}$). Take the recombination rates of the valleys to be the same ($\Gamma_+ = \Gamma_- = \Gamma$) and is equal to the spontaneous emission rate (a) plus intervalley scattering (Γ_v) (*i.e.* $\Gamma = a + \Gamma_v$), with a second-order term (AN_{\pm}) to account for exciton-exciton annihilation, we can write the rate equations as

$$\begin{aligned} \frac{dN_+}{dt} &= -\Gamma N_+ - AN_+^2 - \frac{I_+}{2 I_{\text{sat}}} \Gamma (N_+ - N_{0,+}) + \Gamma_v (N_- - N_+) \\ \frac{dN_-}{dt} &= -\Gamma N_- - AN_-^2 - \frac{I_-}{2 I_{\text{sat}}} \Gamma (N_- - N_{0,-}) + \Gamma_v (N_+ - N_-) \end{aligned} \quad (1)$$

$$N_{\pm} + N_{0,\pm} = N_T$$

where I_{sat} , N_{\pm} , $N_{0,\pm}$ and N_T are saturation intensity and population in the excited, ground states of $\pm K$ valley and total population in each valley, respectively. Solving these equations will give us

population imbalance ($\Delta N = N_+ - N_-$) in the steady-state or transient limits, as shown in the next section.

Next, to connect χ_{vp} to ΔN , we assume

$$\frac{\chi_{vp}}{\chi_{int}} = k_{\chi\mu} \Delta\mu$$

where $k_{\chi\mu}$ is a proportional constant and $\Delta\mu$ is the Fermi level difference between the valleys [1,2]. To connect ΔN to $\Delta\mu$, we first integrate $N = \int_0^\infty D f(E) dE$, where $D = \frac{m^*}{\pi\hbar^2}$ and $f(E)$ are the density of state of MoSe₂ and Fermi-Dirac distribution, which gives $N = Dk_B T \log(1 + e^{\frac{\mu}{kT}})$. The relationship is obtained from $\Delta\mu \approx \frac{\partial\mu}{\partial N} \Delta N$, giving

$$\Delta\mu \approx \frac{k_B}{D} \frac{1}{1 - e^{-\frac{\mu}{kT}}} \Delta N \equiv k_{\mu N}(T) \Delta N.$$

Here we noted that $k_{\mu N}$ increases slowly with temperature, giving us larger sensitivity at higher temperature. Besides, the difference in intensities of σ^+ and σ^- (I_+ and I_- respectively) can be expressed in term of degree of ellipticity, γ (see main text for definition) as $\frac{I_+ - I_-}{I_+ + I_-} = \frac{I_+ - I_-}{I} = \sin(2\gamma)$. Finally, by modelling our experimental setup and procedure described in the Experimental Setup section with Jones matrices, we can get the offset angle of maximum SHG to the system with $\chi_{vp} = 0$ as

$$\begin{aligned} \Delta &\equiv \beta_{\max}(\chi_{vp} \neq 0) - \beta_{\max}(\chi_{vp} = 0) \\ &= \frac{1}{2} \tan^{-1} \left[\frac{2 \frac{\chi_{vp}}{\chi_{int}}}{\left(\frac{\chi_{vp}}{\chi_{int}}\right)^2 - 1} \right]. \end{aligned}$$

We also noted that for experimental procedure in which SHG power analyzed co-linearly with its excitation, the offset angle is $\Delta' = \frac{\Delta}{3}$.

5.1 Steady-state solution

For simplicity, setting the rate equations to be zero for equilibrium condition and $A = 0$, we can get

$$\Delta N = N_+ - N_- = -\frac{2 N_T \Gamma \eta \sin(2\gamma)}{-(2 + \eta)[4 \Gamma_v + \Gamma(2 + \eta)] + \Gamma[\eta \sin(2\gamma)]^2}$$

where $\eta = \frac{I}{I_{\text{sat}}}$. Under the condition where $\Gamma_v = 0$ (which is what we are using, explained below),

we can simplify it to

$$\Delta N_{SS} = N_T \frac{2\eta \sin 2\gamma}{(2 + \eta)^2 - (\eta \sin 2\gamma)^2} \approx N_T \frac{2 \tan 2\gamma \sec 2\gamma}{\eta}$$

for $\eta \gg 1$.

5.1.1 Steady-state solution with $A \neq 0$

We solve the rate equation with no exciton-exciton annihilation term because of its simplicity, such that we can use the form in the transient solution; with it, the overall trend of $\Delta N_{SS,A \neq 0}$ is the same as ΔN_{SS} but scaled by a factor, as illustrated in Figure S4.

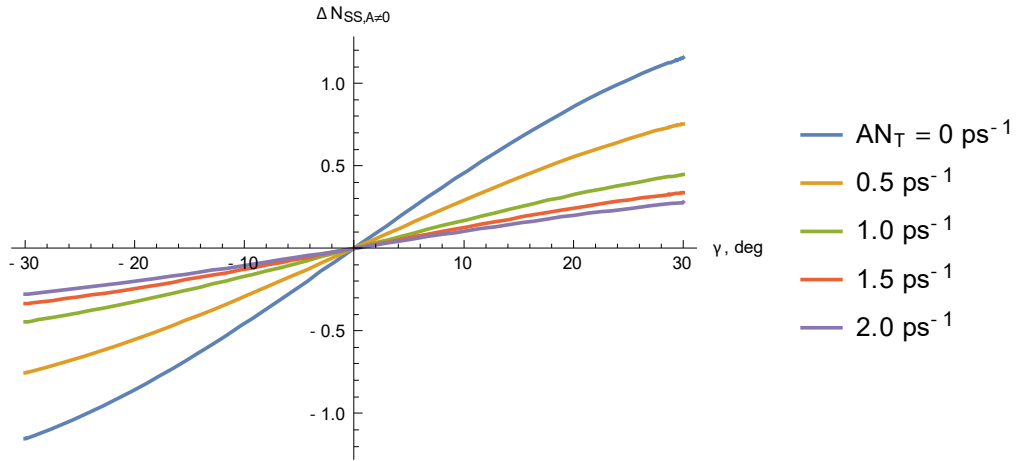


Figure S4: $\Delta N_{SS,A \neq 0}$ with different exciton-exciton annihilation rates.

5.2 Transient solution

However, the steady-state solution does not fully explain our experimental results, as doubling the intensity does not double $\tan(2\Delta)$. Therefore, we moved on to solve the differential equation (1) in addition of $N_{\pm}(t = -\infty) = 0$. For this numerical calculation, unless otherwise stated, we used $\Gamma = 1/3 \text{ ps}^{-1}$ [3], $AN_T = 1.914 \text{ ps}^{-1}$ [4] (N_T appears here because we implicitly normalizing the

rate equations with N_T) and $\Gamma_v = 0$; the latter assumption is justified by that our highest photon energy in excess to PL signal is only 19 meV, which is less than the threshold energy (38 meV for MoSe₂) for phonon-assisted intervalley scattering [5]. Figure S5 shows the calculation results for low, optimum and high intensities.

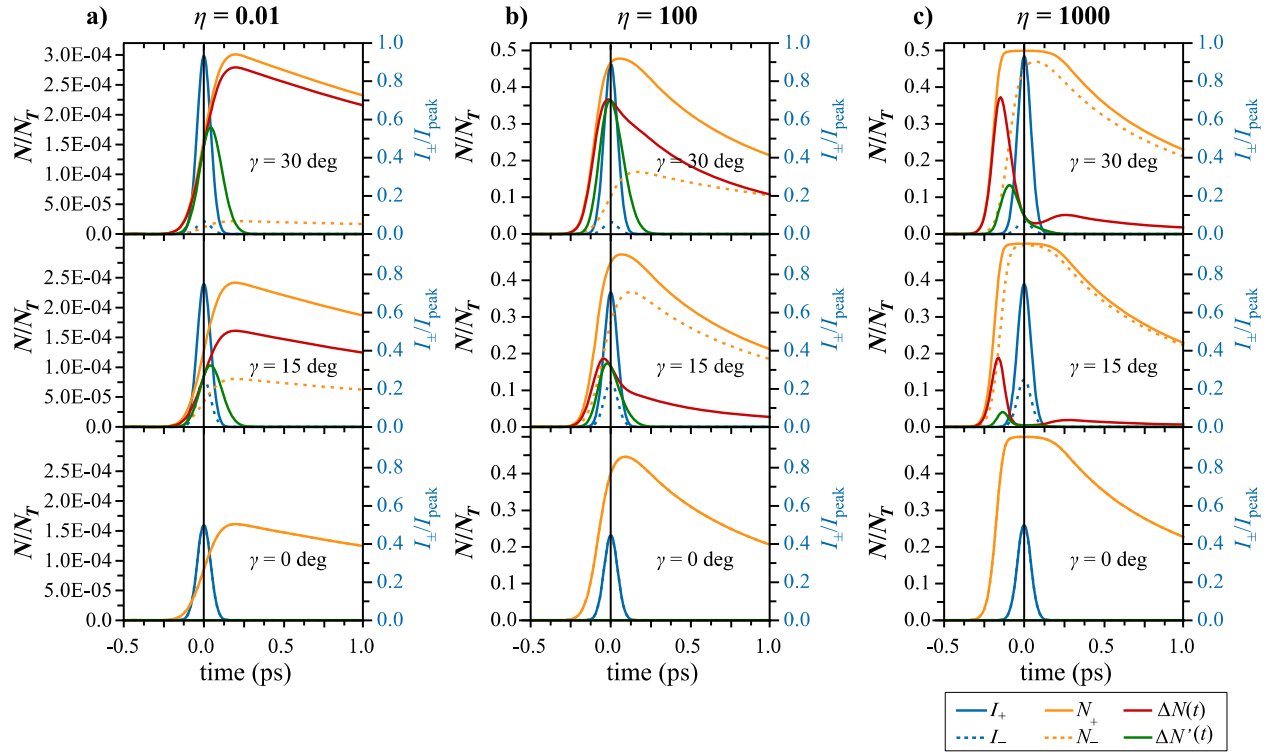


Figure S5: Calculation of populations in $\pm K$ valleys (orange solid and dashed) for $\eta =$ a) 0.01 (low), b) 100 (optimum) and c) 1000 (high intensity) for $\gamma = 30^\circ, 15^\circ$ and 0° . I_{\pm} is the normalized σ^{\pm} intensity, N_{\pm} is the population in $\pm K$ valley, $\Delta N(t) = N_+ - N_-$ is the transient population imbalance and $\Delta N'(t) = \Delta N(t)I(t)$ is the $\Delta N(t)$ normalized with laser pulse.

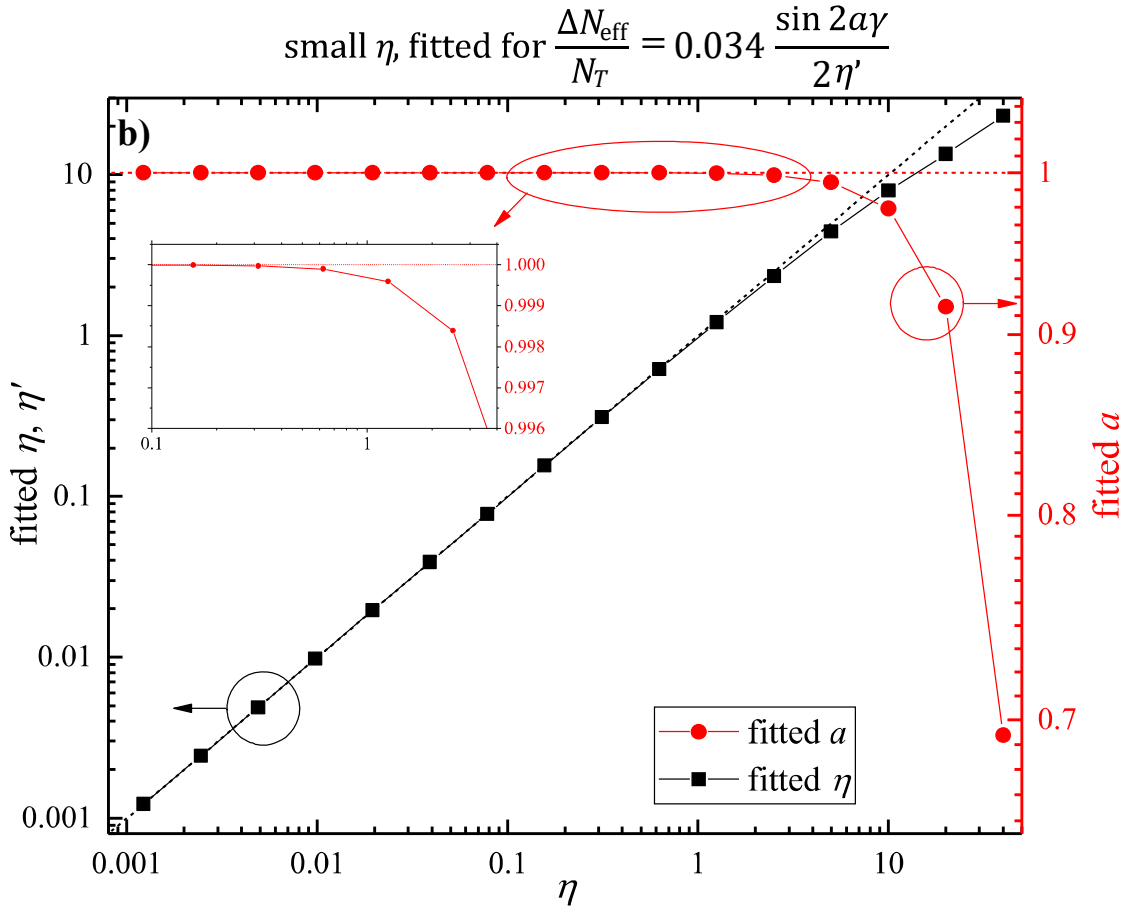
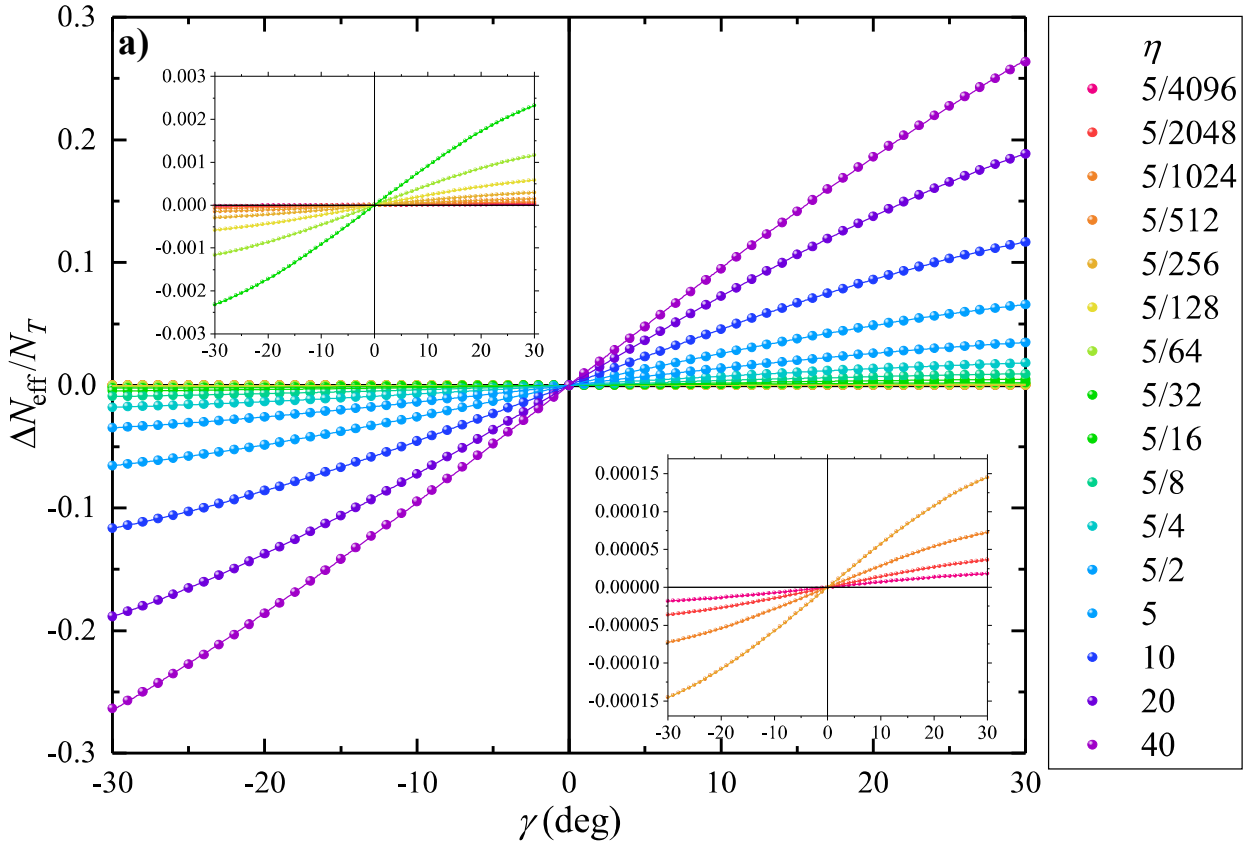
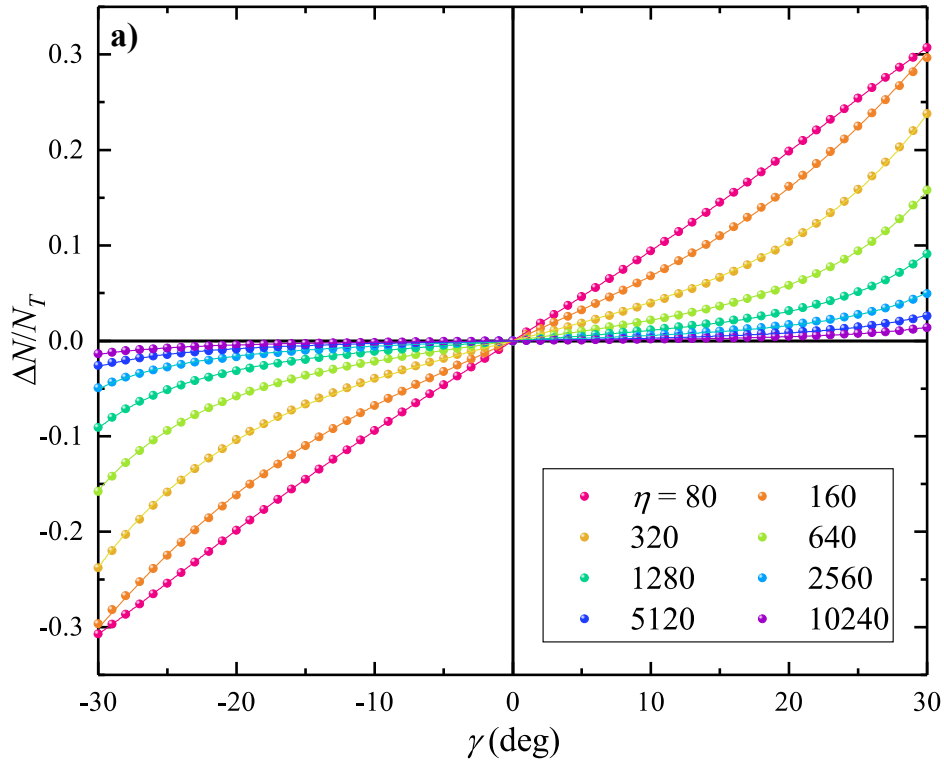


Figure S6: a) Calculation summary of population imbalance as a function of ellipticity for low pump intensities. Insets are the magnified of the figure. Results in a) are fitted to $\frac{0.034}{2\eta'} \sin 2a\gamma$, summarized in b). Inset shows the simplification of ΔN fails when $\eta \gtrsim 0.04$.



large η , global fitted for $\frac{\Delta N_{\text{eff}}}{N_T} = \frac{2\eta' K \sin 2a\gamma}{(2 + \eta')^2 - (\eta' \sin 2a\gamma)^2}$ with $K = 1.058$ and $a = 1.028$

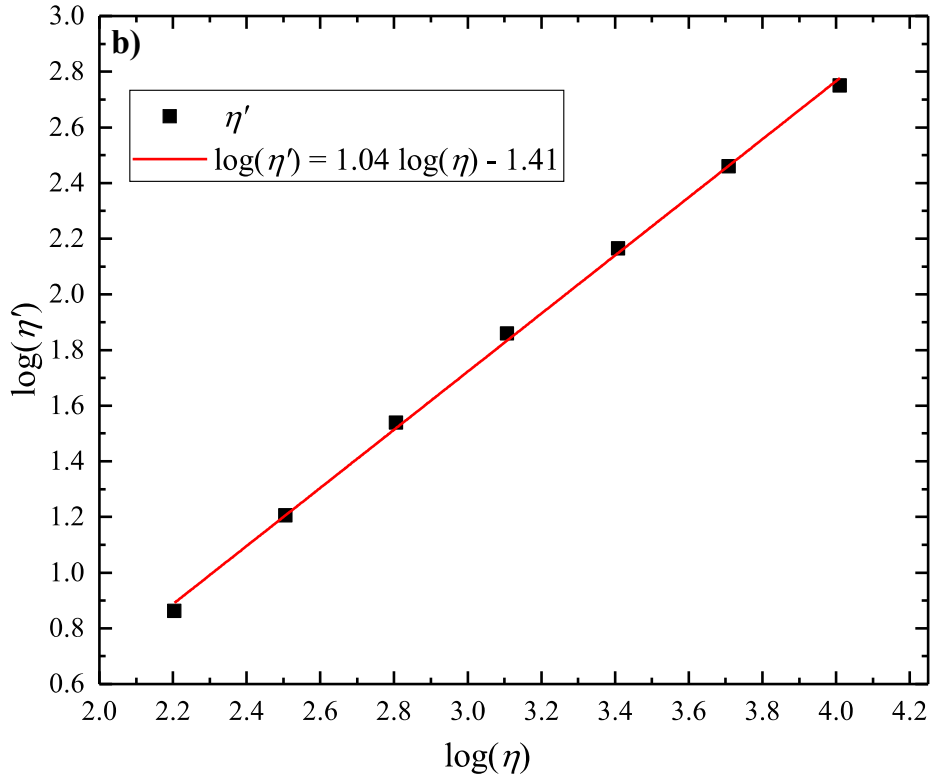


Figure S7: a) Calculation summary of population imbalance as a function of ellipticity for high pump intensities. Results in a) are globally fitted to $\frac{2\eta' K \sin 2a\gamma}{(2 + \eta')^2 - (\eta' \sin 2a\gamma)^2}$ with the global variables $K = 1.058$ and $a = 1.028$, summarized in b). Deviation of $\eta' = \eta$ indicates the steady-state model fails in high intensity regime.

Figure S6 and Figure S7 show the calculation summaries of ΔN as a function of γ for low and high η , respectively. From Figure S6a, we can see that it fits well to the very low intensity approximation of $\Delta N \propto \sin 2\gamma$, which is just the difference in σ^\pm intensities; when $\eta \gtrsim 0.04$ this simplification starts to fail as we can see in Figure S6b, the fitting parameter a in $\sin 2a\gamma$ deviates from unity.

For high η , we fit the results in Figure S7a to the modified version of steady-state ΔN formula of

$$\frac{\Delta N}{N_T} = \frac{2\eta' K \sin 2a\gamma}{(2 + \eta')^2 - (\eta' \sin 2a\gamma)^2}$$

with K and a as global variables. The fitting results are summarized in Figure S7b. The deviation of $a = 1$ indicate steady-state formula fails in high intensity regime. In fact, for $\gamma \ll 1$ and $\eta' \gg 2$, it can be simplified to

$$\frac{\Delta N}{N_T} \approx \frac{4Ka\gamma}{\eta'}$$

Therefore, plotting $\log(\frac{\Delta N}{N_T \gamma})$ against $\log \eta$ gives a linear line as shown in Figure S8, with gradient close but not equal to unity indicates the “effective” intensity η' cannot be described by simply multiplying by a global constant, which in fact has been implied by the non-unity gradient of Figure S7b; enforcing $\eta' \propto \eta$ will give significant deviation as shown in the grey dashed line in Figure S8. We noted that the deviation between the gradients and y-intercepts of Figure S7b and Figure S8 arises from the fitting imperfection.

Figure S9 shows the effect of pulse duration of the laser τ to the population imbalance. At high intensity region, larger τ gives larger response because it delays the onset of saturation, giving larger ΔN_{eff} from integrating $\Delta N(t)$ with respective pulse intensity; graphically, the area under the $\Delta N'(t)$ (solid green) curve in Figure S5 increases with τ .

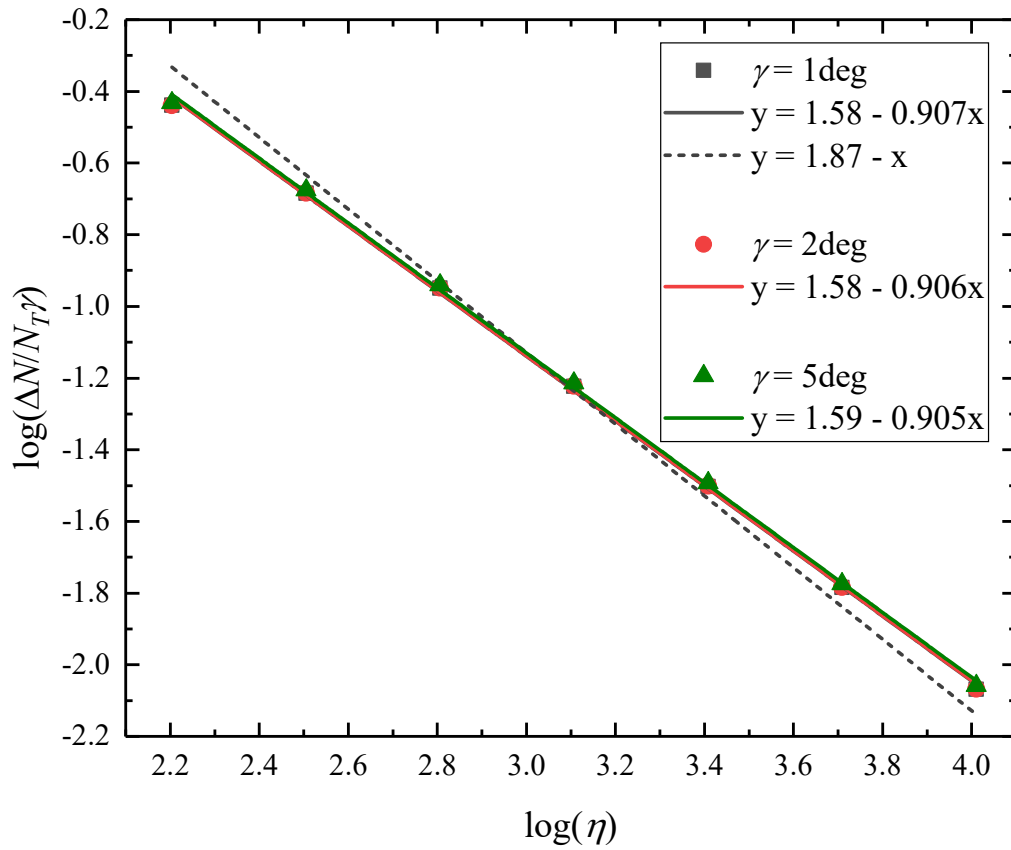


Figure S8: plot of $\log(\frac{\Delta N}{N_T \gamma})$ against $\log \eta$ for small γ . Solid grey and red lines are fitting with fixed y-intercept and gradient, while dashed line is fitting with fixed -1 gradient.

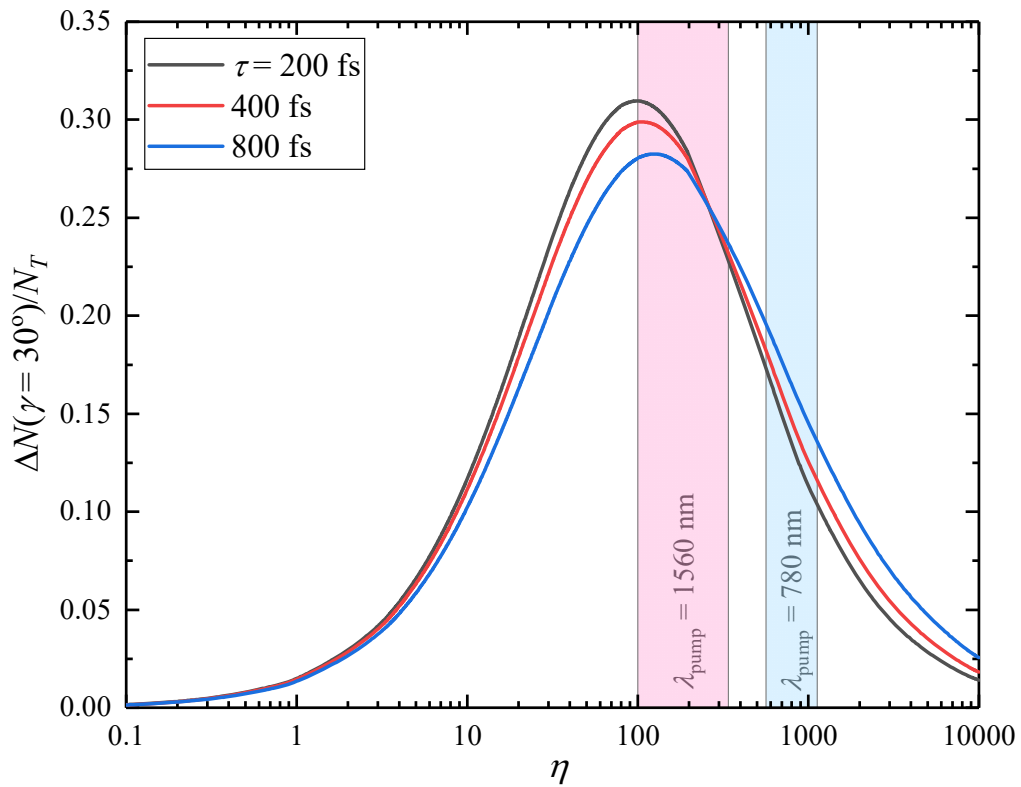


Figure S9: effect of pulse duration of laser τ in the population imbalance response.

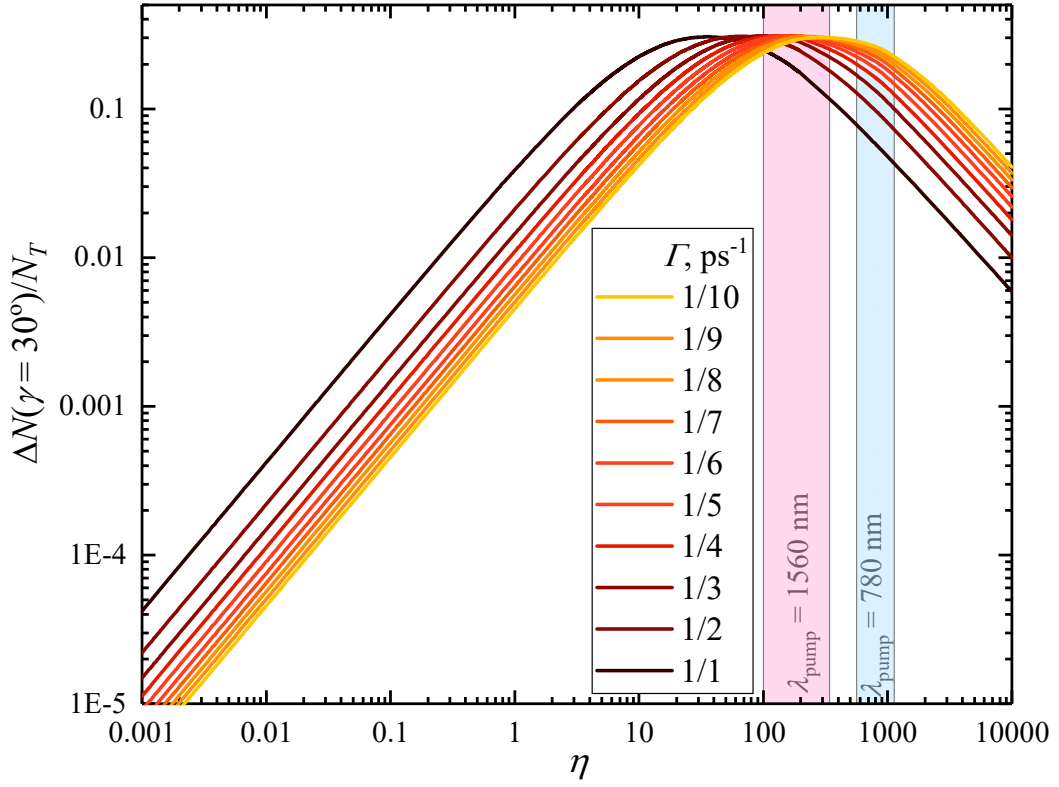


Figure S10: Response of population imbalance as a function of pump intensity for different carrier lifetimes. Experimental working intensity regimes are highlighted in red for 1560 nm and blue for 780 nm pump.

Figure S10 shows the transient calculation for the peak of ΔN in η with various Γ , which translates to sample temperature. The experimental results would be more sensitive for $\lambda_{\text{pump}} = 780$ nm as we reduce the temperature, but this enhancement would be negligible for 1560 nm. Besides, we can see there is a peak response of ΔN in the function of η when $\eta \approx 100$, meaning it is best to carry out experiment with this intensity, but that would need detector with $\sim 10^2$ higher sensitivity for SHG signal for practical data acquisition time.

6 References

1. L. E. Golub and S. A. Tarasenko, "Valley polarization induced second harmonic generation in graphene," *Phys. Rev. B* **90**, 201402 (2014).
2. T. O. Wehling, A. Huber, A. I. Lichtenstein, and M. I. Katsnelson, "Probing of valley polarization in graphene via optical second-harmonic generation," *Phys. Rev. B* **91**, 041404

- (2015).
3. G. Wang, E. Palleau, T. Amand, S. Tongay, X. Marie, and B. Urbaszek, "Polarization and time-resolved photoluminescence spectroscopy of excitons in MoSe₂ monolayers," *Appl. Phys. Lett.* **106**, 112101 (2015).
 4. N. Kumar, Q. Cui, F. Ceballos, D. He, Y. Wang, and H. Zhao, "Exciton-exciton annihilation in MoSe₂ monolayers," *Phys. Rev. B - Condens. Matter Mater. Phys.* **89**, 1–6 (2014).
 5. G. Kioseoglou, A. T. Hanbicki, M. Currie, A. L. Friedman, and B. T. Jonker, "Optical polarization and intervalley scattering in single layers of MoS₂ and MoSe₂," *Sci. Rep.* **6**, 25041 (2016).
 6. K. Wang, Y. Feng, C. Chang, J. Zhan, C. Wang, Q. Zhao, J. N. Coleman, L. Zhang, W. J. Blau, and J. Wang, "Broadband ultrafast nonlinear absorption and nonlinear refraction of layered molybdenum dichalcogenide semiconductors," *Nanoscale* **6**, 10530–10535 (2014).